Article

Effect of Neighboring Transitions on Critical Angle in Conversion between EIA and EIT in 87Rb Atoms

Aisar-ul Hassan , Heung-Ryoul Noh [*] , Jin-Tae Klm [*]

Article

Effect of Neighboring Transitions on Critical Angle in Conversion between EIA and EIT in ^{87}Rb Atoms

Aisar-ul Hassan [1], Heung-Ryoul Noh [2],* and Jin-Tae Kim [1],*

[1]   Department of Photonic Engineering, Chosun University, Gwangju 61452, Republic of Korea
[2]   Department of Physics, Chonnam National University, Gwangju 61186, Republic of Korea
*   Correspondences: hrnoh@chonnam.ac.kr (H.-R.N.); kimjt@chosun.ac.kr (J.-T.K.)

Abstract: The effects of neighboring transitions (ENT) on electromagnetically induced transparency (EIT), electromagnetically induced absorption (EIA), and the conversion between EIA and EIT in a degenerate multi-level system of ^{87}Rb atoms were studied in mmmterms of the angle (θ) between the polarization axes of the coupling and probe beams. The predicted critical values of θ, in which EIT transitioned to EIA, were consistent with the experimental values. In this work these results were systematically confirmed using the calculated spectra by varying the frequency spacings in the excited state of ^{87}Rb via a factor called the ratio. We observed that when the ratio was less than 0.1, the critical angle θ_c was inverted. This may be attributed to the interplay between the strengths of the EIA and EIT as the ENT varied. We also discovered that by modifying the frequency spacings in the excited state of ^{87}Rb, it becomes feasible to predict ENT and the interplay between EIT and EIA in alkali-metal atoms.

Keywords: EIA; EIT; rubidium

---

1. Introduction

Converting between electromagnetically induced absorption (EIA) and electromagnetically induced transparency (EIT) allows the sign of the dispersion slope to be manipulated, which provides exceptional control over the properties of the medium in a coherent manner. However, many studies on how the polarizations [1–4] of the probe and coupling beams depend on the conversion between EIT and EIA have not considered the effects of the neighboring transitions (ENT).

The conversion between the EIA and EIT can be controlled in many ways [5–14]. Reversing the sign of EIT with respect to the polarization ellipticity for the $F = 2 \rightarrow F' = 3$ transition of ^{87}Rb has been investigated without accounting for ENT [15–19]. However, the total absorption of the D2 line incorporating the Doppler effect could not be determined [13]. Gozzini et al. [1] confirmed that the EIT can be tuned continuously to the EIA by choosing right-handedness of the circular polarization and appropriate propagation direction of the coupling and probe beams.

In addition, a theoretical model for a graphene metastructure featuring switchable properties between EIT and EIA within a three-resonator system has been developed [10]. Chanu et al. [14] showed that an N-type formation using two control beams enabled to the conversion from EIT to EIA. Depending on the various polarization combinations, EIT or EIA can be formed such that it is possible to make a convert between EIA and EIT. Moreover, the angle dependence of the polarization axes of the coupling and probe beams on EIA and EIT in ^{85}Rb atoms caused by ENT [20] (in which EIT or EIA can occur) has been reported. However, the switching mechanism for alkali-metal atoms is still not well known. The ENT in adjacent multi-level systems, combined with a change in the angles between the polarization axes of the coupling and probe beams, is important in the mechanisms that convert between EIT and EIA.

In this study the ENT and angle θ between the polarization axes of the coupling and probe beams in the $F = 2 \rightarrow F' = 1, 2, 3$ transitions of ^{87}Rb are investigated. The critical angle θ_c was measured and calculated in cases in which EIT could be converted into EIA. We also found that the ENT can be derived from the critical angles obtained by artificially varying the spacings of the excited states of ^{87}Rb because the conversion between EIA and EIT strongly depends on the ENT. We also found that

by adjusting the frequency spacings in the excited state of ^{87}Rb, it becomes possible to predict ENT and the competition between EIT and EIA in alkali-metal atoms including ^{87}Rb atom.

The rest of this paper is organized as follows. Section 2 derives the theoretical calculation for ^{87}Rb. Section 3 describes the experimental setup. Section 4 presents the experimental and calculated results. Section 5 discusses the results, and Section 6 contains the conclusion.

2. Theoretical Calculation

The energy level diagram for ^{87}Rb is shown in Figure 1, in which the blue (red) arrow and "0" ("δ_d") represent the transitions excited by the coupling (probe) beam and its relative frequency, respectively (δ_d is defined below). To examine the ENT in the EIA or EIT spectra, we intentionally varied the frequency spacings in the excited state. In this case, the frequency spacings shown in Figure 1 vary by a common factor defined as the ratio (see Figure 7 in Section 5).
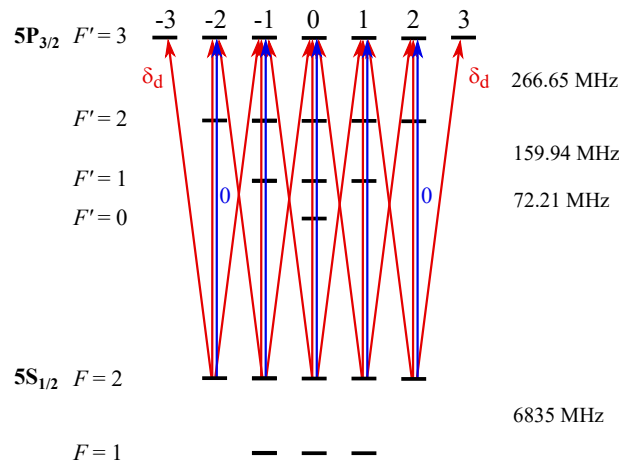

Figure 1. Energy level diagram for the $F = 2 \rightarrow F' = 1, 2,$ and 3 transitions of the ^{87}Rb D2 line. The blue and red lines indicate the transitions excited by the coupling and probe beams, respectively.

Both the coupling and probe beams were linearly polarized, and their polarization axes differed by an angle θ. Because the power of the coupling beam was larger than that of the probe beam by a factor of 3.3 in the experiment, we selected the polarization axis of the coupling beam as the quantization axis. Selecting the polarization axis of the probe beam as the quantization axis is also possible, but in this case, we need to use higher interactions than the three photons, normally used in the calculation, can provide to guarantee sufficient accuracy. In the spherical bases, the polarization axes of the coupling and probe beams are given by $\hat{e}_0$ and $a_{+1}\hat{e}_+ + a_0\hat{e}_0 + a_{-1}\hat{e}_-$, respectively, where

$$a_{\pm 1} = \mp 2^{-1/2}\sin\theta \quad \text{and} \quad a_0 = \cos\theta. \tag{1}$$

Therefore, the coupling beam excited the transitions with $\Delta m = 0$, whereas the probe beam excites the transitions with $\Delta m = 0$ and ± 1, as shown in Figure 1.

The density matrix equation for the $F = 2 \rightarrow F' = 1, 2,$ and 3 transitions of the ^{87}Rb D2 line is given by

$$\dot{\rho} = -(i/\hbar)[H, \rho] + \dot{\rho}_{\text{relax}}, \tag{2}$$

where ρ is the density operator, $\dot{\rho}_{\text{relax}}$ is the term associated with the relaxation phenomena [21]. The Hamiltonian (H) in Equation (2) is expressed as

$$H = -\sum_{F'=1}^{3}\sum_{m=-F'}^{F'} \hbar(\delta_c + \Delta_{3F'})|F',m\rangle\langle F',m|$$

$$+\frac{\hbar}{2}\Omega_p e^{-i\delta_d t}\sum_{q=-1}^{1}\sum_{F'=1}^{3}\sum_{m=-2}^{2} a_q C_{2,m}^{F',m+q}|F',m+q\rangle\langle F,m|$$

$$+\frac{\hbar}{2}\Omega_c\sum_{F'=1}^{3}\sum_{m=-2}^{3} C_{2,m}^{F',m}|F',m\rangle\langle F,m| + \text{h.c.}, \tag{3}$$

where $\delta_c \equiv d_c - kv$, $\delta_d \equiv d_p - d_c$, d_c (d_p) is the detuning of the coupling (probe) beam, k is the wave vector, v is the velocity of an atom, and $\Delta_{3F'}$ is the frequency spacing between the states $|F'=3\rangle$ and $|F'\rangle$. In Equation (3), Ω_p (Ω_c) is the Rabi frequency of the probe (coupling) beam, h.c. represents the Hermitian conjugate, and $C_{F,m}^{F',m'}$ is the normalized transition strength between the states $|F',m'\rangle$ and $|F,m\rangle$ [22].

The density matrix elements should be expanded into several terms that oscillate at different oscillation frequencies. The expansions of the density matrix elements between the excited and ground states, the excited and excited states (and the ground and ground states), and the populations are given by Eqs. (5)–(7) and Eqs. (8) and (9), and Eq. (10) in [20], respectively

A series of coupled time-dependent differential equations, obtained by inserting the Hamiltonians and expanded density matrix elements into Equation (2), was solved for the steady-state regime. Then, the final absorption coefficient, averaged over the Maxwell–Boltzmann velocity distribution, is given by

$$\alpha = -\frac{3\lambda^2}{2\pi}\frac{N_{\text{at}}}{\Omega_p}\int_{-\infty}^{\infty}\frac{\mathrm{d}v}{\sqrt{\pi}v_{\text{mp}}}e^{-(v/v_{\text{mp}})^2}$$

$$\times\text{Im}\left[\sum_{j=1}^{3}\sum_{q=-1}^{1}\sum_{m=-2}^{2} a_q^* C_{2,m}^{F',m+q}\langle F',m+q|\rho^{(1)}|F,m\rangle\right], \tag{4}$$

where λ is the wavelength of the laser, v_{mp} is the most probable speed of the atoms, and N_{at} is the atomic density in the cell. $\langle F',m+q|\rho^{(1)}|F,m\rangle$ is the decomposed matrix element of $\langle F,m+q|\rho|F,m\rangle$ oscillating as $e^{-i\delta_d t}$. To perform a quantitative analysis of the ENT on the spectra, we performed two types of calculations: degenerate two-level system (DTLS) calculation and degenerate multi-level system (DMLS) calculation. In the DMLS (DTLS) calculation, all neighboring hyperfine states were taken into account (neglected).

3. Experimental Setup

A laser beam with wavelength of 780 nm from a tunable external cavity diode laser (DLpro, Toptica Inc.) was transmitted through an optical window; a small portion of the laser beam was reflected for saturated absorption spectroscopy, and the rest was sent to a polarizing beam splitter (PBS-1), as shown in Figure 2. A half-wave plate (HWP) was placed before PBS-1 to divide the beam into coupling and probe beams and to maintain the beam power ratio between the two resulting beams. The probe beam was expanded by 5–6 mm in diameter using a beam expander (GBE05-B, Thorlabs), and the beam was aimed at the vapor cell after it passed through the beam splitter (BS). The HWP placed before the BS maintained the polarization of the probe beam. The vapor cell was 5 cm in length and 2.5 cm in diameter. The vapor cell is protected from the effects of stray magnetic fields and Earth's magnetic field by five layers of μ-metal sheet. The coupling beam was scanned by passing it through two acousto-optic modulators (AOM). The first AOM, labeled AOM-1 (3080-122, Gooch & Housego) was fixed at 80 MHz using the AOM driver (1080AF-AINA-1.0 HCR, Gooch & Housego), and the other AOM, labeled AOM-2 (3080-122, Crystal Technology, Inc.), was scanned within ± 1 MHz at -80 MHz using the deflector driver (DE-802EM26, IntraAction). To match the polarization of the probe beam

(P-polarized), another set of HWPs and PBSs were used for the coupling beam. A beam expander (GBE05-B, Thorlabs) was used to expand the coupling beam to a diameter of 6 mm. Both the probe and coupling beams met at the BS;to specify θ, and the HWP was placed in the path of the coupling beam before it reached the BS. For 10 different settings of HWPs placed before the BS, spectral profiles were recorded for the $F = 2 \rightarrow F' = 1, 2$ and 3 transitions of ^{87}Rb.
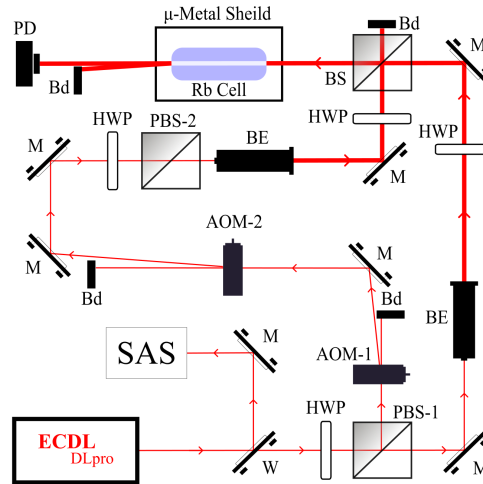

Figure 2. Schematic of the experimental setup. SAS: saturated absorption spectroscopy; W: window; HWP: half-wave plate; PBS: polarizing beam splitter; BE: beam expander; AOM: acousto-optic modulator; M: mirror; BS: beam splitter; Bd: beam dump; PD: photodetector.

4. Experimental and Calculated Results

The calculated spectra for the DTLS and DMLS and the experimental spectra for the transitions from the upper-ground hyperfine energy level $F = 2$ of the D2 line of ^{87}Rb are shown in Figures 3–5, respectively. The closed $F = 2 \rightarrow F' = 3$ transition exhibited EIT instead of EIA at $\theta = 0°$. However, the open $F = 2 \rightarrow F' = 2$ and $F = 2 \rightarrow F' = 1$ transitions exhibited EIAs at larger θ, as shown in Figures 3c, 4c, and 5c.
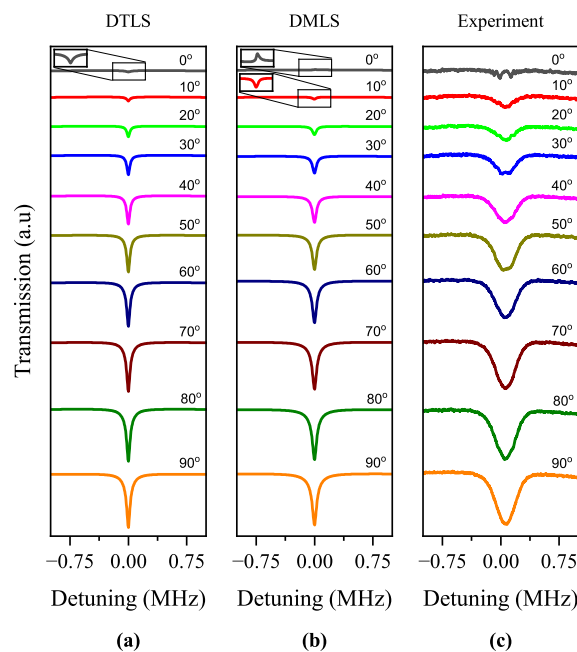

Figure 3. Calculated spectra for the (a) DTLS (b) DMLS, and (c) experimentally measured spectra for the resonant $F = 2 \rightarrow F' = 3$ transition.
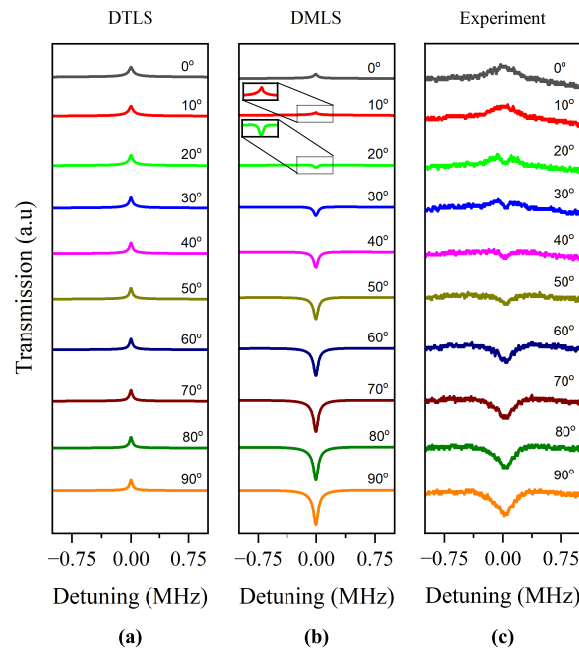
Figure 4. Calculated spectra for the (a) DTLS (b) DMLS, and (c) experimentally measured spectra for the resonant $F = 2 \rightarrow F' = 2$ transition.
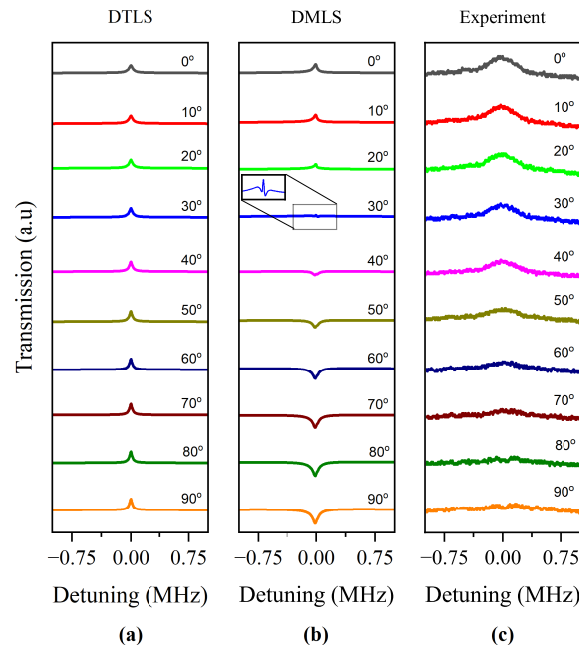

Figure 5. Calculated spectra for the (a) DTLS (b) DMLS, and (c) experimentally measured spectra for the resonant $F = 2 \rightarrow F' = 1$ transition.

The calculated spectra for the DTLS and DMLS and experimental spectra for the closed $F = 2 \rightarrow F'$ = 3 transition are shown in Figure 3a–c, respectively. Instead of EIA, EIT appeared at $\theta = 0°$. The EIT switched to EIA at $\theta = 10°$. After the switch to EIA, the amplitudes of the EIA increased as θ increased. The maximum EIA amplitude appeared at $\theta = 90°$, as shown in Figure 3c. The experimental spectra were consistent with the calculated spectra for the DMLS, as shown in Figure 3b, with EIT at $\theta = 0°$. The influence of the open $F = 2 \rightarrow F' = 2$ and $F = 2 \rightarrow F' = 1$ transitions resulted in EIT at $\theta = 0°$. This was why the calculated spectra for the DTLS that neglected the contributions from neighboring

transitions for the closed $F = 2 \rightarrow F' = 3$ transition had EIAs at all θ, as shown in Figure 3a. The calculated EIA spectra for the DTLS also increased in amplitude as θ increased.

For the open $F = 2 \rightarrow F' = 2$ transition, the amplitudes of the EIT increased as θ increased for the DTLS calculation with relatively small amplitudes, as shown in Figure 4a. Because of the dominance of the closed $F = 2 \rightarrow F' = 3$ transition, the calculated EIT spectra for the DMLS switched to EIA at $\theta = 20°$, as shown in Figure 4b. Similarly, the experimental spectra shown in Figure 4c reflect the conversion of EIT to EIA. After switching, the EIA amplitude increased as θ increased, and the maximum amplitude occurred at $\theta = 90°$. The EIT, in contrast, had a maximum amplitude at $\theta = 0°$ for both calculated spectra for the DMLS and experimental spectra.

For the $F = 2 \rightarrow F' = 1$ transition, the amplitude of the EIT increased as θ increased for the calculated spectra for the DTLS, as shown in Figure 5a. This transition is further away from the $F = 2 \rightarrow F' = 3$ transition because hyperfine splitting was large, which was why the EIT switched to EIA at a larger θ compared to the $F = 2 \rightarrow F' = 2$ transition for the calculated spectra for the DMLS shown in Figure 5b. The EIT switched to EIA at a larger angle, as shown in Figure 5c, and was not consistent with the DMLS spectra. A plausible reason for this discrepancy is given in Section 5 using a small variation of the transmission at θ.

5. Discussion

To accurately determine the critical θ, the line-center transmission with respect to the transmission of the broad spectrum was plotted as a function of θ. The experimental and calculated results are shown in Figure 6a,b, respectively. The experimental values of the critical angle for the $F = 2 \rightarrow F' = 3, 2$, and 1 transitions were measured to be 3.7°, 15.9°, and 75.1°, respectively. To accurately determine the theoretical critical θ, a 1° interval near the critical angle was used instead of a 10° interval. The calculated values were 3.5°, 16.7°, and 37.5°, respectively. Thus, the experimental and calculated results were in good agreement, except for the $F = 2 \rightarrow F' = 1$ transition. In the experiment, the line-center transmission values gradually increased as θ increased, and this trend was also observed in the calculated results. The experimental line-center transmission of the $F = 2 \rightarrow F' = 1$ transition line deviated from the theoretical expectation. This discrepancy can be explained as follows: as is readily seen in Figure 6b, the variation in the transmission at θ for the $F = 2 \rightarrow F' = 1$ transition was very small compared to those for the $F = 2 \rightarrow F' = 2, 3$ transitions. Thus, the critical angle may have been inaccurately determined.
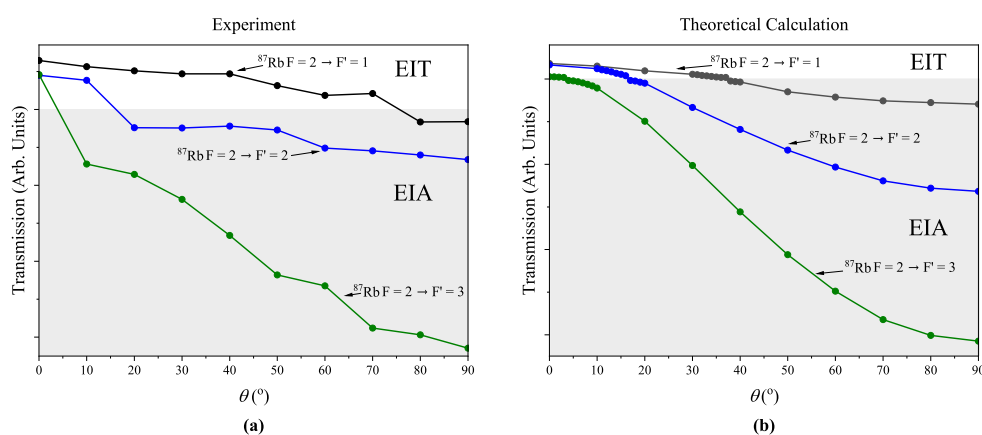

Figure 6. (a) Experimental and (b) theoretical line–center transmission values with respect to θ for the $F = 2 \rightarrow F' = 1, 2$, and 3 transitions.

The critical angles θ_c displayed in Figure 7 show the strength of the ENTs in the EIA and EIT spectra. Compared to the results for ^{85}Rb reported in [20], the critical angles for the $F \rightarrow F' = F, F - 1$ transitions of ^{87}Rb were larger than those of ^{85}Rb, and vice versa for the $F \rightarrow F' = F + 1$ transition.

In this work to investigate this phenomenon more systematically, we calculated the critical angles by intentionally varying the frequency spacings in the excited state of ^{87}Rb using a factor called the ratio. For example, if the ratio was unity, the critical angles corresponded to the values for pure ^{87}Rb, as shown in Figure 7. In contrast, if the ratio was to 0.5, the frequency spacings were reduced to half that of ^{87}Rb. In this case, the neighboring effect increased compared to the case of ^{87}Rb.
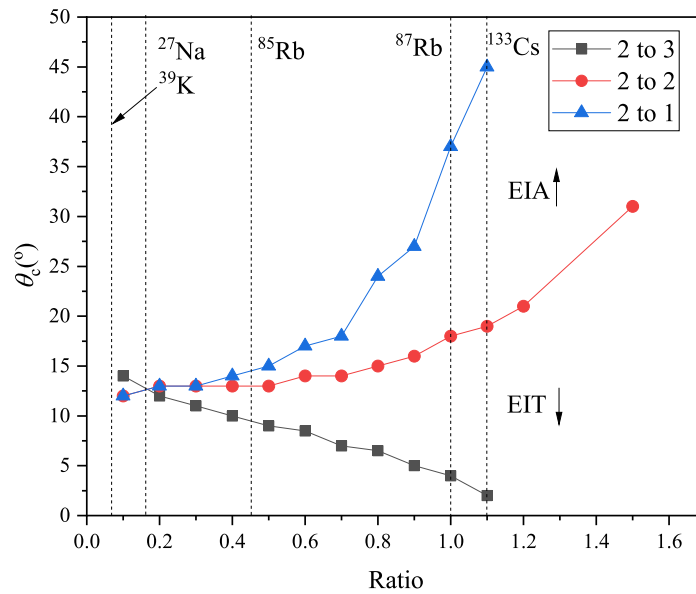

Figure 7. Critical angles (θ_c) versus the strength of the ENT on the EIA and EIT spectra.

The calculated results are presented in Figure 7. The critical angles for the $F = 2 \to F' = 1, 2$, and 3 transitions are displayed from top to bottom as a function of the ratio. As the ratio increased, the critical angles for the $F = 2 \to F' = 1, 2$ transitions ($F = 2 \to F' = 3$ transition) increased (decreased) monotonically. The calculation of θ_c was not accurate, unlike in typical critical phenomena. This occurred because, when the EIT was converted into the EIA, the introduction of the EIA was gradual rather than radical. However, because our aim was to determine only the overall trend of the transmissions, an inaccurate determination of θ_c did not impact the results of this study.

Because the conversion between the EIA and EIT strongly depends on the ENT rather than the energy level structure, the behavior of other atomic species can be easily predicted by changing the frequency spacings. More accurately, the ENT depends on the frequency spacing divided by the natural linewidth of the transition, which is regarded as the effective frequency spacing. In Figure 7 the values $\Delta_{F+1,F}/\Gamma$ are presented as vertical dotted lines. For example, the critical angles for ^{133}Cs were larger (smaller) for the $F \to F' = F - 1, F$ transitions ($F \to F' = F + 1$ transition) than those for ^{87}Rb. We expect that the conversion between EIA and EIT occurs for other atomic species in a similar way.

For the $F \to F' = F + 1$ transition, as θ changed from 0 to θ_c, the strong transitions between the $|F, m = \pm F\rangle$ and $|F' = F + 1, m' = \pm(F + 1)\rangle$ states began to produce the EIA signal. The EIT was converted to the EIA at $\theta = \theta_c$. If the ratio was decreased (i.e., the ENT was increased) while θ was fixed at θ_c, then the effect of the $F \to F' = F$ transition on the $F \to F' = F + 1$ transition increased, and the signal changed to EIT accordingly. Thus, θ_c increased as the ratio decreased as shown in Figure 7.

For the $F \to F' = F$ and $F - 1$ transitions, the conversion from EIT to EIA occurred at a larger value of θ because of the off-resonant contribution of the strong $F \to F' = F + 1$ transition. In this case, as the ratio decreased (i.e. as the ENT increased), the signal changed to EIA owing to the effect of

the $F \to F' = F + 1$ transition. Thus, θ_c decreased as the ratio decreases, in contrast to the case of the $F \to F' = F + 1$ transition.

For the $F \to F' = F + 1$ transition, only the EIA could be observed when the ratio was larger than approximately 1.2. In this case, the ENT was not sufficient to convert EIA into EIT. When the ratio was very large, which corresponded to the case in which the ENT was absent, only the EIA for the $F \to F' = F + 1$ transition and the EIT for the $F \to F' = F$ and $F - 1$ transitions could be observed. This corresponded exactly to the calculation for the DTLS.

In Figure 7, the inversion of θ_c can be observed for ratio values smaller than approximately 0.1, (i.e., a larger θ_c was observed for the $F \to F' = F + 1$ transition than the $F \to F, F - 1$ transitions.) This phenomenon may have resulted from the interplay between the strength of the EIA owing to the transitions between the $|F, m = \pm F\rangle$ and $|F' = F + 1, m' = \pm(F + 1)\rangle$ states and that of the EIT owing to the $F \to F, F - 1$ transitions when the ENT increased. To examine this phenomenon more quantitatively, we calculated the spectra for the $F \to F' = F + 1$ transition when the ratios were 0.1 and 1.0 accounting for all the ENT and excluding the effect of the $F \to F' = F - 1$ transition.

The results for the ratios of 0.1 and 1.0 at $\theta = \theta_c$ are shown in Figure 8a,b, respectively. In Figure 8, the black curves represent the spectra accounted for all the neighboring transitions and the red curves represent the spectra that considered only the $F \to F' = F$ transition (i.e., neglected the $F \to F' = F - 1$ transition). The angles were $\theta_c = 14°$ and $4°$, as shown in Figure 8a,b, respectively. In Figure 8a, the strengths of the EIT and EIA were comparable for the black curve, and the effect of the EIT was weaker than that of the EIA for the red curve. In contrast, as shown in Figure 8b, the effect of the $F \to F' = F - 1$ transition was very weak because of the larger hyperfine spacing. Thus, when the ratio was 0.1, the effect of the EIT was enhanced owing to the neighboring transitions associated with the EIT, and a larger θ needed to be converted from EIT to EIA. Thus, we could observe larger θ_c for the $F \to F' = F + 1$ transition when the ratio was smaller than approximately 0.1.
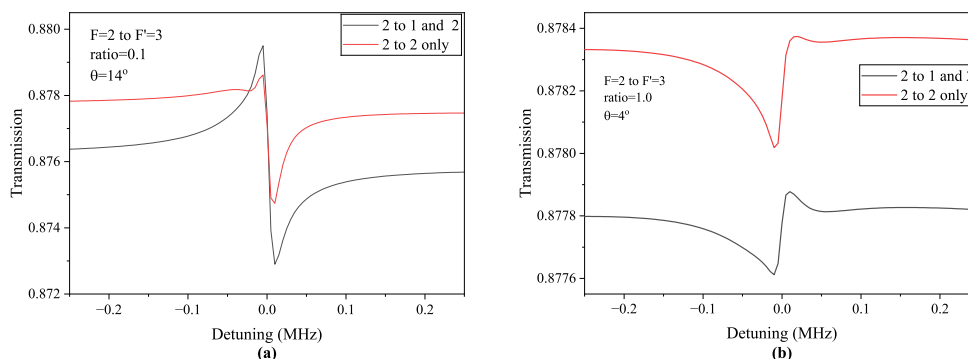

Figure 8. The spectral results for the ratio of (a) 0.1 with $\theta_c = 14°$ and (b) 1.0 with $\theta_c = 4°$ for the $F = 2 \to F' = 3$ transition. The black curves represent the spectra that accounted for all the neighboring transitions and the red curves represent the spectra that considered only the $F = 2 \to F' = 1$ transition.

6. Conclusions

In this study, the ENT on EIA, EIT, and the conversion between EIA and EIT in ^{87}Rb atoms were investigated in terms of the angle between the polarization axes of the coupling and probe beams. The observed spectral profiles were compared to the calculated absorption profiles by considering the ENT. The results were consistent with the observed spectra for all the transitions. The slight quantitative disagreement for the $F = 2 \to F' = 1$ transition was explained by accounting for the weak variation in the transmission for θ.

EIT (instead of EIA) occurred at smaller θ for the upper hyperfine ground state of ^{87}Rb, and the amplitude of the EIA increased as θ increased for all the $F = 2 \to F' = 1, 2$, and 3 transitions after the transformation from EIT to EIA. The theoretical critical θ, at which EIT is converted to EIA, was consistent with the experimentally measured critical θ values except for the $F = 2 \to F' = 1$ transition. Compared to ^{85}Rb, the critical angles for the $F \to F' = F, F - 1$ transitions in ^{87}Rb were

greater, whereas for the $F \rightarrow F' = F + 1$ transition, the critical angles were smaller. We observed an inversion of the critical angle θ_c when the ratio was smaller than 0.1, resulting in a larger θ_c for the $F \rightarrow F' = F + 1$ transition compared to the $F \rightarrow F'$ and $F - 1$ transitions. This phenomenon was explained by accounting for the competition between the strengths of the EIA and EIT as the ENT varied. The results of this study can deepen our understanding of the ENT on EIA and EIT spectra, and can support useful predictions of the spectra for alkali-metal atoms other than ^{87}Rb atoms.

Author Contributions: Conceptualization, J.K. and H.N.; methodology, A. H.; formal analysis, J.K. and H.N.; investigation, A. H., J. K., H. N..; writing—original draft preparation, A. H., J. K., H. N.; writing—review and editing, J. K., H. N.; supervision, J. K.; project administration, J. K., H. N.; funding acquisition, J. K., H. N.

Institutional Review Board Statement: Not applicable.

Informed Consent Statement: Not applicable.

Data Availability Statement: Not applicable.

Conflicts of Interest: The authors declare no conflicts of interest.

References

1. S. Gozzini, A. Fioretti, A. Lucchesini, L. Marmugi, C. Marinelli, S. Tsvetkov, S. Gateva, S. Cartaleva,Tunable and polarization-controlled high-contrast bright and dark coherent resonances in potassium. *Opt. Lett.* **2017**, *42*, 2930–2933.

2. L.S. Molella, K. Dahl, R.-H. Rinkleff, K. Danzmann, Coupling-probe laser spectroscopy of degenerate two-level systems: An experimental survey of various polarisation combinations.*Opt. Commun.* **2009**, *282*, 3481–3486.

3. D. McGloin, M.H. Dunn, D.J. Fulton, Polarization effects in electromagnetically induced transparency. *Phys. Rev. A* **2000**, *62*, 053802–1-6.

4. N. Ram, M. Pattabiraman, Sign reversal of Hanle electromagnetically induced absorption with orthogonal circularly polarized optical fields. *J. Phys. B: At. Mol. Opt. Phys.* **2010**, *43*, 245503–1-7.

5. C.J. Gao, H.F. Zhang, Switchable Metasurface with Electromagnetically Induced Transparency and Absorption Simultaneously Realizing Circular Polarization-Insensitive Circular-to-Linear Polarization Conversion. *J. Ann. Phys.* **2022**, *534*, 2200108–220013.

6. Y. Lv, D.-D. Zhu, Y.-Z. Sun, D. Zhang, and H.-F. Zhang, Transition from electromagnetically induced transparency to electromagnetically induced absorption utilizing phase-change material vanadium dioxide based on circularly polarized waves. *Physica E: Low dimensional systems and nanostructure* **2023**, *145*, 115507–115526.

7. H. Yu, J. D. Kim, T. Y. Jung, and J. B. Kim, Transformation of EIA to EIT by incoherent pumping of the ^{85}Rb D1 line. *J. Kor. Phys. Soc.* **2012**, *61*, 1227–1231.

8. M. Bhattarai, V. Bharti, and V. Natarajan, Tuning of the Hanle effect from EIT to EIA using spatially separated probe and control beams. *Sci. Rep.* **2018**, *8*, 7525–1-8.

9. Y. Yin, Y. Lv, Y. Sun, and H. Zhang, Tunable conversion of electromagnetically induced transparency to electromagnetically induced absorption based on vanadium dioxide metastructure. *Optik* **2024**, *296*, 171554–171560.

10. D.-D. Zhu, Y. Lv, Y.-Z Sun, H.-F. Zhang, Switching of electromagnetically induced transparency and absorption of graphene metastructure with the three resonators. *Waves in Random and Complex Media* **2023**, *0*, 1–25.

11. I.-H. Bae, H. S. Moon, M.-K. Kim, L. Lee, and J. B. Kim, Transformation of electromagnetically induced transparency into enhanced absorption with a standing-wave coupling field in an Rb vapor cell. *Opt. Express* **2010**, *18*, 1389–1397.

12. C.-J. Yi, M.-C. Shen, Q. Qin, Y.-F. Zhang, X.-M. Lin, and M.-Y. Ye, Transition from electromagnetically-induced transparency to absorption in a single microresonator. *Opt. Express* **2023**, *31*, 7167–7174.

13. R.S. Grewal, M. Pattabiraman, Hanle electromagnetically induced absorption in open $F_g \to F_e \le F_g$ transit ions of the ^{87}Rb D2 line. *J. Phys. B: At. Mol. Opt. Phys.* **2015**, *48*, 085501–1-10.

14. S.R. Chanu, K. Pandey, V. Natarajan, Conversion between electromagnetically induced transparency and absorption in a three-level lambda system. *Europhys. Lett.* **2012**, *98*, 44009–1-6.

15. Z.A.S. Jadoon, H.R. Noh, J.T. Kim, Effects of neighboring transitions on the mechanisms of electromagnetically induced absorption and transparency in an open degenerate multilevel system. *Sci. Rep.* **2022**, *12*, 145–1-9.

16. Z.A.S. Jadoon, A.-u. Hassan, H.R. Noh, J.T. Kim, Effects of neighboring transitions on electromagnetically induced absorption and transparency in ^{85}Rb atoms based on the linear parallel polarization of coupling and probe beams. *Opt. Commun.* **2022**, *520*, 128512–1-5.

17. Z.A.S. Jadoon, A.-u. Hassan, H.R. Noh, J.T. Kim, Electromagnetically induced absorption in Rb atoms with circular polarization of laser beams: Effects of neighboring transitions. *Heliyon* **2022**, *8*, 11752–1-5

18. A.-u. Hassan, Z.A.S. Jadoon, H.R. Noh, J.T. Kim, Effects of neighboring transitions on electromagnetically induced absorption and transparency in Rb atoms in circular orthogonal polarization configuration. *J. Kor. Phys. Soc.* **2023**, *82*, 907–911.

19. Z.A.S. Jadoon, A.-u. Hassan, H.R. Noh, J.T. Kim, Effects of neighboring transitions on electromagnetically induced absorption and transparency in ^{87}Rb atoms with respect to varying hyperfine spacings. *J. Opt. Soc. Am. B* **2023**, *40*, 2612–2617.

20. A.-u. Hassan, H.-R Noh, and J. T. Kim, Angle dependence between the polarization axes of the coupling and probe beams on electromagnetically induced absorption and transparency in ^{85}Rb atoms due to neighboring effect. *Optik* **2024**, *311*, 171906–1-10.

21. G.W. Choi, H.R. Noh, Line shapes in sub-Doppler DAVLL in the ^{87}Rb-D2 line. *Opt. Commun.* **2016**, *367*, 312–315.

22. G.W. Choi, H.R. Noh, Sub-Doppler DAVLL spectra of the D1 line of rubidium: a theoretical and experimental study. *J. Phys. B: At. Mol. Opt. Phys.* **2015**, *48*, 115008–1-11.